High electronic excitation-induced crystallization in $Fe_{73.5}Cu_1Nb_3Si_{13.5}B_9$ amorphous alloy: I. Irradiation with swift heavy monoatomic projectiles

2004 J. Phys.: Condens. Matter 16 1547

(http://iopscience.iop.org/0953-8984/16/9/004)

INSTITUTE OF PHYSICS PUBLISHING JOURNAL OF PHYSICS: CONDENSED MATTER

J. Phys.: Condens. Matter **16** (2004) 1547–1561 PII: S0953-8984(04)71424-1

High electronic excitation-induced crystallization in $Fe_{73.5}Cu_1Nb_3Si_{13.5}B_9$ amorphous alloy: I. Irradiation with swift heavy monoatomic projectiles

G Rizza[1,3], A Dunlop[1], G Jaskierowicz[1] and M Kopcewicz[2]

[1] Laboratoire des Solides Irradiés, Commissariat à l'Energie Atomique/DRECAM/ Ecole Polytechnique/CNRS, 91128 Palaiseau Cedex, France
[2] Institute of Electronic Materials Technology, Wolczynska 133, 01-919 Warszawa, Poland

E-mail: rizza@hp1sesi.polytechnique.fr

Received 6 November 2003
Published 20 February 2004
Online at stacks.iop.org/JPhysCM/16/1547 (DOI: 10.1088/0953-8984/16/9/004)

Abstract

We present a detailed study of the crystallization induced in an amorphous alloy by monoatomic projectiles in the electronic energy deposition regime. The crystallization phenomenon was investigated by transmission electron microscopy (TEM) for different lead ion energies (0.7–5 GeV), irradiation temperatures (80–300 K) and ion fluences (from 1×10^{11} up to 2×10^{13} ions cm^{-2}).

1. Introduction

The slowing down of very energetic heavy projectiles mainly leads to electronic excitation and ionization of the target atoms along the path of the projectiles. The resulting damage depends on the nature of the target and on the amount of energy deposited in electronic processes. It has been shown that a spectacular macroscopic deformation (∼10%) of the samples, called anisotropic growth, appears in all the amorphous targets that have already been studied [1–4]. This effect is observed if the linear rate of energy deposition in electronic processes by the projectile is sufficient, i.e. above a threshold $S_e^{th} \sim 10$ keV nm^{-1} and above a critical irradiation fluence Φ_c. The samples shrink along the beam direction and expand perpendicular to the beam direction. It is now accepted [5, 6] that during the incubation period damage is introduced in the amorphous structure along the path of each projectile, leading to the creation of additional free volume and thus of cylinders of 'modified' amorphous matter.

The recent discovery of the partial crystallization of the $Fe_{73.5}Cu_1Nb_3Si_{13.5}B_9$ amorphous alloy induced by high electronic energy deposition [7], indicates that the very general scheme for damage creation described above does not apply to all amorphous alloys. In this paper we present a detailed study of a crystallization process induced in an amorphous alloy

[3] Author to whom any correspondence should be addressed.

irradiated by GeV monoatomic ions. We analyse the effect of swift heavy ion irradiation on the phase transformation in $Fe_{73.5}Cu_1Nb_3Si_{13.5}B_9$ amorphous alloy and we try to draw a scheme for the irradiation-induced crystallization. For this study we selected amorphous $Fe_{73.5}Cu_1Nb_3Si_{13.5}B_9$ alloy which has attracted a lot of attention because it serves as a precursor for the formation of the soft magnetic nanocrystalline phase [8]. This amorphous alloy crystallizes upon annealing in two steps. When the annealing temperature exceeds the crystallization temperature corresponding to the first peak (at about 520 °C) in the differential scanning calorimetry (DSC) curve, a nanostructure is formed which consists of nanograins of Fe(Si) phase with a well-defined grain size (∼10 nm) embedded in a residual amorphous matrix. Such a nanocrystalline alloy (called Finemet) reveals excellent soft magnetic properties. Increase of the annealing temperature above the second crystallization peak (at about 670 °C) in the DSC curve causes a complete crystallization of the amorphous matrix as a result of which the size of Fe(Si) grains increases and iron borate compounds (Fe_2B, Fe_3B, $Fe_{23}B_6$, ...) are formed. At the same time, the soft magnetic properties dramatically deteriorate [8–11]. As this alloy is characteristic of a particular class of amorphous alloys exhibiting two-step crystallization, it would be interesting to study the behaviour of such an alloy submitted to high electronic energy deposition.

2. Experimental details

The samples used in this study are amorphous $Fe_{73.5}Cu_1Nb_3Si_{13.5}B_9$ ribbons prepared by the melt spinning technique. The targets in the form of 3 mm diameter discs were electrochemically pre-thinned for transmission electron microscopy (TEM) observations. They were mounted in a liquid nitrogen cryostat installed on the GANIL accelerator line and irradiated with 5 GeV and 700 MeV incident Pb ions at normal incidence under a controlled ion flux ($<5 \times 10^8$ ions cm^{-2} s^{-1}) in order to limit the temperature increase of the samples under the beam (irradiation temperature always stayed well below 90 K). The linear rate of energy deposition of these Pb ions in $Fe_{73.5}Cu_1Nb_3Si_{13.5}B_9$ alloy in electronic processes is respectively $S_e \sim 40$ and 50 keV nm^{-1} (see table 1). Samples irradiated at fluences of 1×10^{11}–2×10^{13} ions cm^{-2} were slowly heated up to room temperature and examined in a 300 keV transmission electron microscope (Philips CM 30). Observations of amorphous targets irradiated with swift heavy ions allow the visualization by TEM of the surface deformations on both sample surfaces [12, 13]. These permit the determination of the cross-sections of the cylinders of *modified* matter. Observations were performed using the phase contrast technique, which consists of defocusing the objective lens of the microscope to give rise to a phase contrast (Fresnel fringes) inside the ion deformed regions (tracks). High-resolution transmission electron microscopy (HRTEM) micrographs were processed with a slow-scan CCD camera and analysed with the digital micrograph program. The TEM observations were always performed using a very low electron flux in order to avoid any structural modification of the sample induced by the electron beam. The projectiles used, fluences and linear rates of energy deposition in electronic processes of the various ions in $Fe_{73.5}Cu_1Nb_3Si_{13.5}B_9$ alloy are reported in table 1.

3. Experimental results

3.1. Unirradiated sample

Figure 1(a) shows a bright field electron micrograph of an unirradiated sample. As expected, no contrast is visible. The electron diffraction pattern (figure 1(b)) is characteristic of an

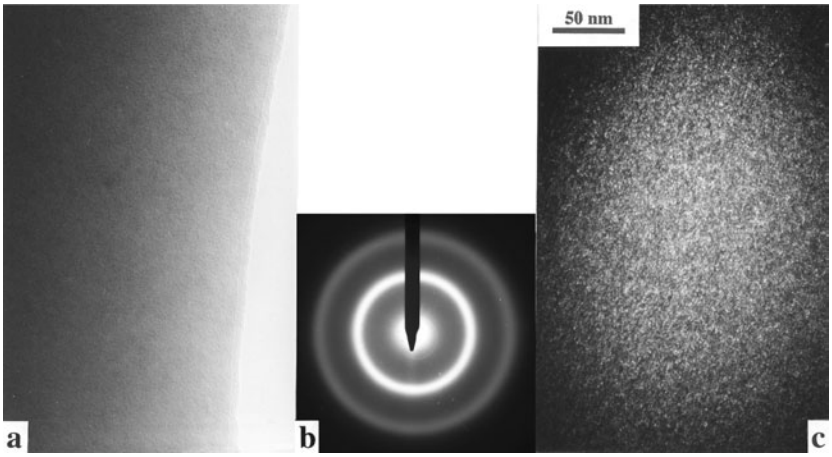

Figure 1. Transmission electron micrograph (a) and corresponding electron diffraction pattern (b) of an unirradiated $Fe_{73.5}Cu_1Nb_3Si_{13.5}B_9$ amorphous sample (diffuse rings A1 and A2). (c) A dark field image obtained using the first diffuse ring A1.

Table 1. The most important parameters concerning the irradiation with GeV lead ions: figure numbers, ion energy (GeV), average linear rate of energy deposition in electronic processes (keV nm^{-1}), irradiation temperature (K) and ion fluence (ions cm^{-2}).

Sample (figures)	Energy (GeV)	S_e (keV nm^{-1})	T^{irr} (K)	Fluence (ions cm^{-2})
A Figures 2–4, 14	5	40	80	10^{11}
B Figures 5, 6	5	40	300	10^{11}
C Figure 7	0.7	50	300	10^{11}
D Figures 8, 9	5	40	80	10^{12}
E Figure 10	5	40	80	2×10^{13}
F Figure 11	0.7	50	300	2×10^{12}
G Figure 12	0.7	50	300	8×10^{12}

amorphous alloy. It consists of two very wide diffraction rings, hereafter referred to as A1 and A2. The first one, A1, is centred at a position corresponding to an *interplanar distance* $d = 2.033$ Å, which according to the Guinier formula [14] corresponds to an average distance x_m in the amorphous structure $x_m = 1.23d = 2.50$ Å. This value agrees with the determination of Hampel *et al* [15], giving $x_m = 2.5$ Å. Figure 1(c) is a dark field image obtained using the first diffuse ring A1. The image consists of an assembly of small dots of typical sizes ∼1 nm, which characterize an amorphous structure [16].

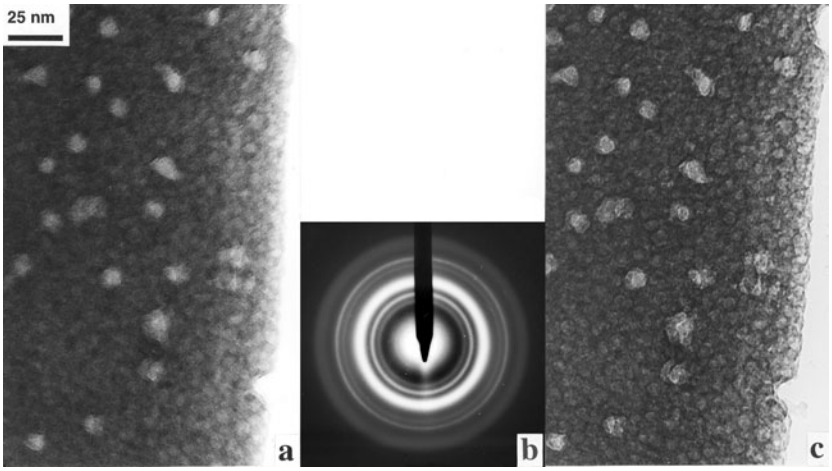

Figure 2. Bright field transmission electron micrographs ((a) and (c) in focused and slightly defocused conditions) of an $Fe_{73.5}Cu_1Nb_3Si_{13.5}B_9$ amorphous sample irradiated at normal incidence at 80 K with 5 GeV Pb ions up to a fluence of 10^{11} ions cm^{-2}. The corresponding electron diffraction pattern is given in (b) (four crystalline rings).

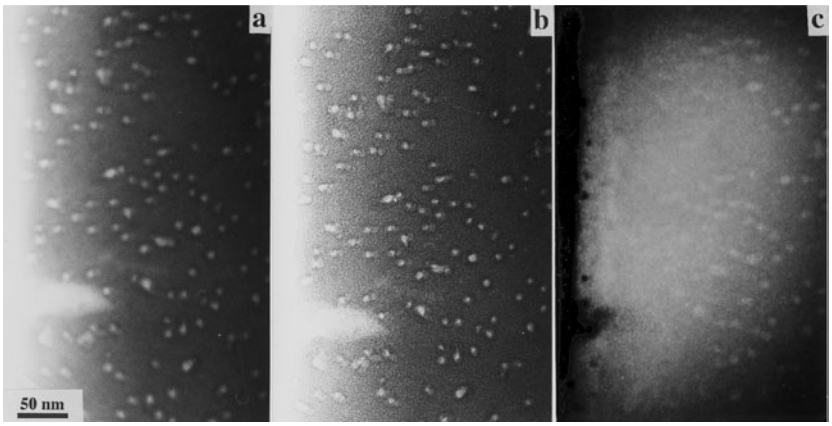

Figure 3. Bright field transmission electron micrographs ((a) and (b) in focused and slightly defocused conditions) of an $Fe_{73.5}Cu_1Nb_3Si_{13.5}B_9$ amorphous sample irradiated at normal incidence at 80 K with 5 GeV Pb ions up to a fluence of 10^{11} ions cm^{-2}. (c) A dark field image obtained using the first diffuse ring A1.

3.2. Irradiation at low fluences

The main results deduced from TEM observations of $Fe_{73.5}Cu_1Nb_3Si_{13.5}B_9$ samples, corresponding to targets irradiated up to 1×10^{11} Pb ions cm^{-2} are collected in the upper part of table 2. The corresponding TEM micrographs and electron diffraction patterns are presented in figures 2– 7. All the diffraction rings observed throughout the study are schematically reported in figure 13.

3.2.1. Irradiation at 80 K with 5 GeV lead ions up to 1×10^{11} *ions* cm^{-2}. Figure 2(a) shows a bright field electron micrograph obtained in focused conditions. White spots of rather irregular shape associated with the impacts of the projectiles are clearly visible. The density of these

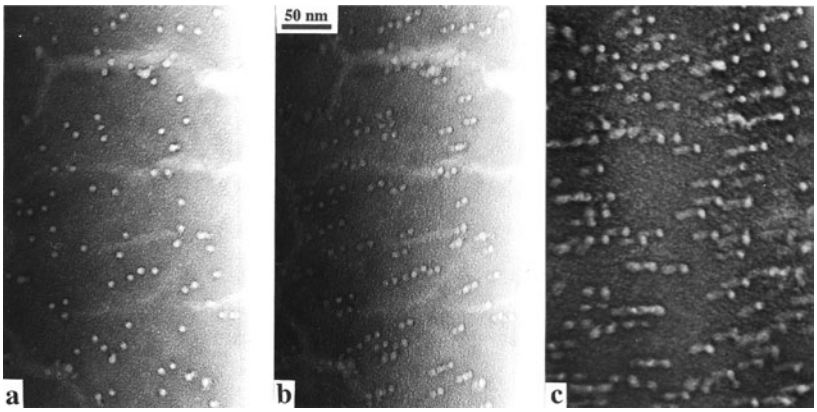

Figure 4. Bright field transmission electron micrographs obtained in slightly defocused conditions in an $Fe_{73.5}Cu_1Nb_3Si_{13.5}B_9$ amorphous sample irradiated at normal incidence at 80 K with 5 GeV Pb ions up to a fluence of 10^{11} ions cm^{-2}. Tilt angles: 0° for (a), 10° for (b) and (c).

Table 2. Important results concerning the inner diameter of the damaged regions, the observed crystalline diffraction rings and microdiffraction rings and most probable corresponding phases.

Sample	Inner diameter (nm)	Comments	Crystalline diffraction rings (possible phases)	Microdiffraction rings (possible phases)
A	6.8–7.5	1. Surface deformations (sometimes contrast in the bulk) 2. Amorphous matter in the track core	C1(Fe_2B) C2($Fe_{23}B_6$) C3($Fe_{23}B_6$) C4($Fe_{23}B_6$)	
B	8.2	1. Surface deformations 2. Amorphous matter in the track core 3. Nanocrystalline matter at the periphery	C1(Fe_2B) C2($Fe_{23}B_6$) C4($Fe_{23}B_6$)	
C	12.5	Surface deformations	C1(Fe_2B) C4($Fe_{23}B_6$)	
D		1. Ragged sample edge 2. Amorphous matter in the track core	C2($Fe_{23}B_6$) C4($Fe_{23}B_6$)	μ1($Fe_{23}B_6$) μ2($Fe_{23}B_6$) μ3($Fe_{23}B_6$) μ4($Fe_{23}B_6$) μ5
E		Anisotropic growth near the central hole	No cryst. rings	μ6($Fe_{23}B_6$) μ7($Fe_{23}B_6$)
F		Anisotropic growth near the central hole	No cryst. rings	
G		Anisotropic growth near the central hole	No cryst. rings	

spots corresponds to the ion fluence, which indicates that each projectile locally induces some 'damage' which is visible by TEM. The observed diameters of the impact zones range from 6.8 to 7.5 nm. In out-of-focus conditions (figure 2(c)), using the phase contrast technique

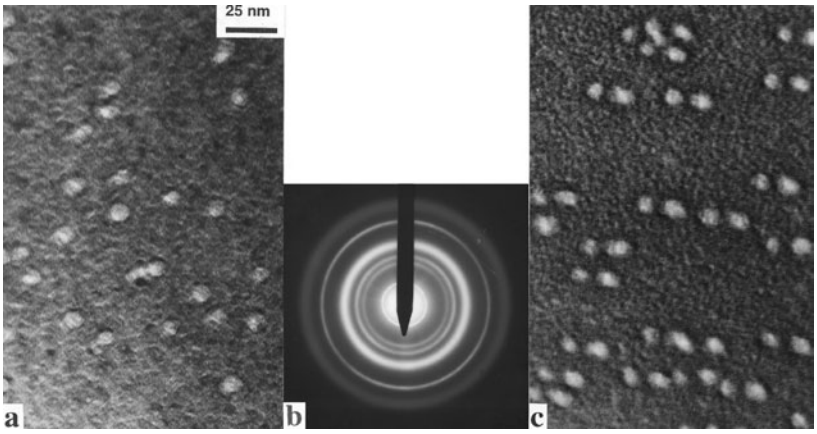

Figure 5. Bright field electron micrographs obtained in slightly defocused conditions in an $Fe_{73.5}Cu_1Nb_3Si_{13.5}B_9$ amorphous sample irradiated at normal incidence at 300 K with 5 GeV Pb ions up to a fluence of 10^{11} ions cm^{-2}. Tilt angle is 15° in (c). Three crystalline rings are seen in the electron diffraction pattern, (b).

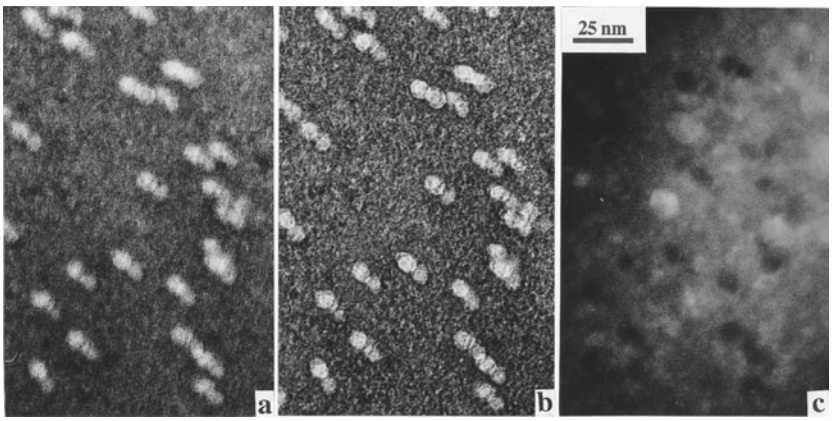

Figure 6. Bright field transmission electron micrographs ((a) and (b) in focused and slightly defocused conditions) of an $Fe_{73.5}Cu_1Nb_3Si_{13.5}B_9$ amorphous sample irradiated at normal incidence at 300 K with 5 GeV Pb ions up to a fluence of 10^{11} ions cm^{-2}. Tilt angle 10°. (c) A dark field image obtained using a distant crystalline ring.

which allows the visualization of local variations of the sample thickness, the contrast is strongly increased. The corresponding electron diffraction pattern (figure 2(b)) shows big differences in comparison with the original one (figure 1(b)). The two diffuse rings (A1 and A2) characteristic of the amorphous structure as well as four thin continuous rings (hereafter named C1–C4, see figure 13 below) characteristic of crystalline matter are clearly seen. Two of them (C1 and C2) correspond to radii smaller than that of the first amorphous ring A1, two others (C3 and C4) are located between rings A1 and A2.

In figure 3, related again to a sample irradiated up to a fluence of 1×10^{11} ions cm^{-2}, a dark field image (figure 3(c)) obtained using the first diffuse ring A1, shows that in addition to the small dots characteristic of an amorphous structure, which are seen over all the sample surface, a white contrast is seen at the impact sites. This suggests that amorphous matter is still present in the core of the tracks.

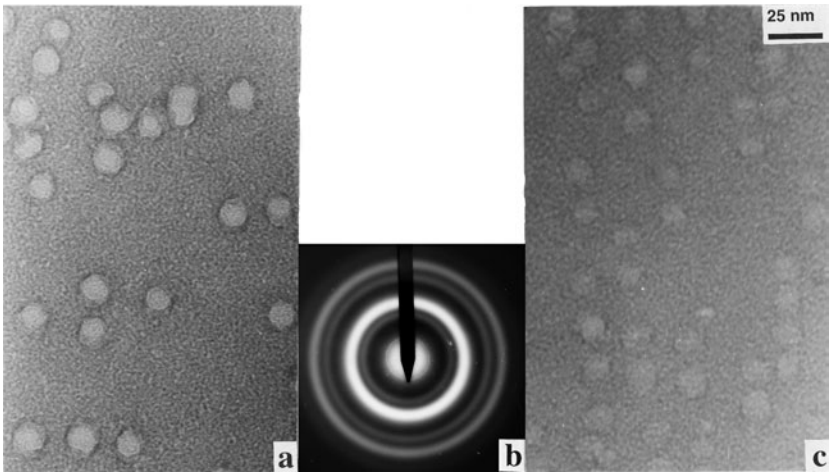

Figure 7. Bright field transmission electron micrographs in slightly defocused conditions of an $Fe_{73.5}Cu_1Nb_3Si_{13.5}B_9$ amorphous sample irradiated at normal incidence at 300 K with 0.7 GeV Pb ions up to a fluence of 10^{11} ions cm^{-2}. Tilt angle 40° in (c). Two crystalline rings are visible on the corresponding electron diffraction pattern (b).

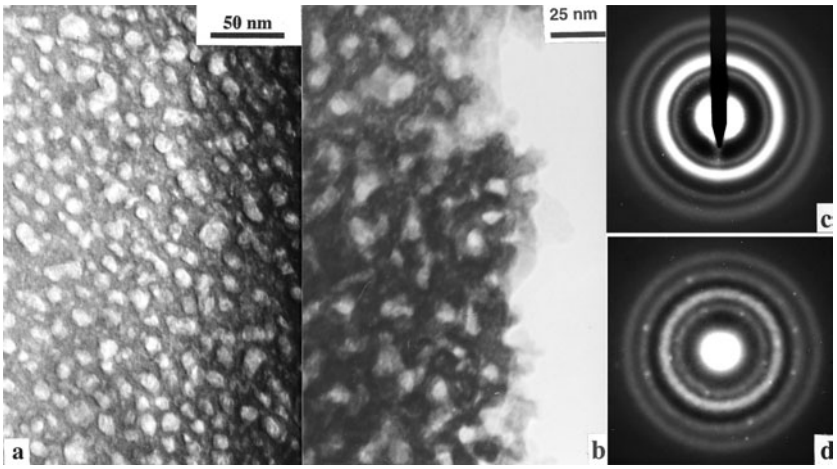

Figure 8. Bright field transmission electron micrographs (a, b) of an $Fe_{73.5}Cu_1Nb_3Si_{13.5}B_9$ amorphous sample irradiated at normal incidence at 80 K with 5 GeV Pb ions up to a fluence of 10^{12} ions cm^{-2}. Two crystalline rings are visible on the corresponding electron diffraction pattern (c). A microdiffraction pattern obtained from a nanosized region at an impact site is shown in (d).

Finally, in figure 4, we visualize the same tracks seen from the top (tilt angle 0° in the microscope in figure 4(a)) and when the sample has been tilted by 10° in the electron microscope (figures 4(b) and (c)). Figure 4(b) shows that the contrast is mainly visible on both sample surfaces (white dots circled in black due to observations in slightly defocused conditions). In a few rare cases it was possible to image some faint contrast in the bulk of the sample, as shown in figure 4(c), on which an almost continuous contrast is visible along the path of the projectile through the sample thickness.

3.2.2. Irradiation at 300 K with 5 GeV lead ions up to 1×10^{11} *ions cm*$^{-2}$. The experimental results obtained changing the irradiation temperature from 80 to 300 K and using the same projectile and the same fluence as above, are described in this section. Figure 5(a) shows individual impact zones. When the sample is tilted in the electron microscope (figure 5(c)), it is again observed that the contrast is mainly located on both sample surfaces. The contrasts observed on the surfaces consist of bright spots of an average diameter of 8.2 nm, surrounded by black circles. They are clearly associated with the formation of hollows surrounded by protruding rims, similar to the surface deformations previously observed in irradiated amorphous Ni_3B [12, 13]. The corresponding electron diffraction pattern (figure 5(b)) shows the two diffuse rings A1 and A2 and three strong crystalline rings (labelled above as C1, C2 and C4). In addition, some much weaker crystalline rings of much larger diameter are observed. Figure 6 shows some tracks observed after tilting the sample by 10° in the electron microscope. Figure 6(c) is a dark field image obtained using selected area diffraction (SAD) on a crystalline ring, which is far from the central diffraction spot. It is clear that the core of the tracks remains black, whereas 4–5 nm diameter black dots are visible between the tracks. *This could indicate that the track core remains amorphous and that nanocrystallization occurs outside the track cores, at larger distances from the ion paths*.

3.2.3. Irradiation at 300 K with 700 MeV lead ions up to 1×10^{11} *ions cm*$^{-2}$. We now check the influence of the rate of energy deposition on the nature of the damage created. We compare previous results obtained after irradiations at low fluences at room temperature with lead ions of 5 GeV with those observed using 700 MeV projectiles. The linear rate of energy deposition in $Fe_{73.5}Cu_1Nb_3Si_{13.5}B_9$ is increased from 40 to 50 keV nm^{-1} (table 1). Figure 7 shows the impact zones of the slow projectiles observed with tilt angles of 0° (figure 7(a)) and 40° (figure 7(c)) in the electron microscope. The observed damaged regions now have more regular circular cross-sections with an average inner diameter increased to 12.5 nm. Contrast is once more mainly visible on both sample surfaces. On the corresponding electron diffraction pattern (figure 7(b)) two crystalline rings (C1 and C4) are clearly visible in addition to the diffuse rings characteristic of the amorphous structure.

3.3. Irradiation at high fluences

3.3.1. Irradiation at 80 K with 5 GeV lead ions.

Irradiation up to 1×10^{12} *ions cm*$^{-2}$. No quantitative information can be deduced concerning the sizes of individual damaged regions from the bright field micrographs (figure 8(a) in a thick region of the sample, figure 8(b) on the edge of the sample near the central hole), because there is already a strong spatial overlap of the damaged regions at such a fluence. It is clear that some strong irregularities are observed on the edge of the sample: they will be described in more detail below. The electron diffraction pattern (figure 8(c)) shows the coexistence of two amorphous rings, A1 and A2, and of two (C2 and C4) of the thin crystalline lines previously observed. Figure 8(d) shows a microdiffraction pattern which was obtained by using a convergent electron beam in order to select the smallest possible area of the irradiated target centred on one of the damaged regions. This mode allows the contribution to the diffraction pattern of the undamaged amorphous material located between the irradiated regions to be minimized. In figure 8(d), one can observe an intensity modulation on five rings (quoted as $\mu 1$–$\mu 5$ in figure 13) which comes from the superposition of small diffraction spots originating from crystalline regions. One of them ($\mu 2$, see figure 13) is located at a radial distance located inside the diffuse amorphous ring A1. The others are clearly located outside the amorphous

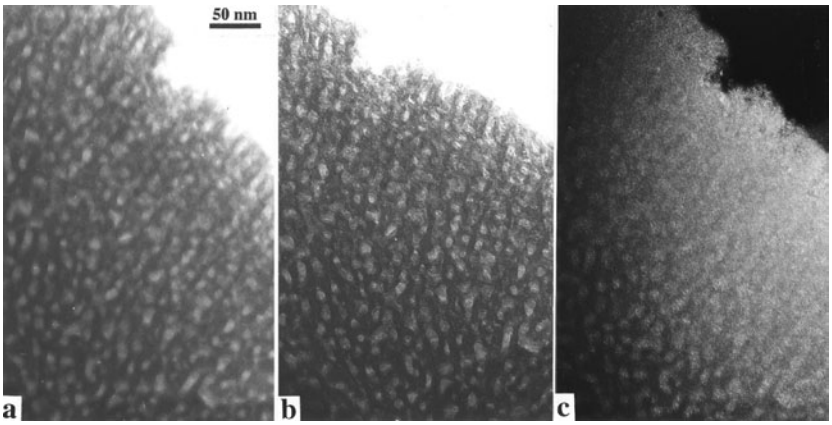

Figure 9. (a, b) Bright field transmission electron micrographs in slightly defocused conditions of an $Fe_{73.5}Cu_1Nb_3Si_{13.5}B_9$ amorphous sample irradiated at normal incidence at 80 K with 5 GeV Pb ions up to a fluence of 10^{12} ions cm^{-2}. (c) A dark field image obtained using the first diffuse ring A1.

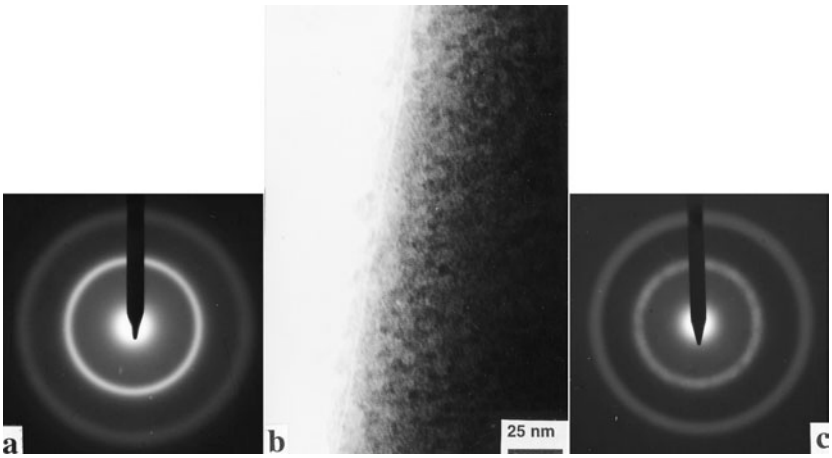

Figure 10. Bright field transmission electron micrograph (b) of an $Fe_{73.5}Cu_1Nb_3Si_{13.5}B_9$ amorphous sample irradiated at normal incidence at 80 K with 5 GeV Pb ions up to a fluence of 2×10^{13} ions cm^{-2}. No crystalline rings are visible on the corresponding electron diffraction pattern (a). A microdiffraction pattern is shown in (c).

rings as shown in figure 13. The dark field image, obtained using the SAD on the first diffuse ring A1, (figure 9(c)) shows once again that amorphous matter is still present in the core of the tracks.

Irradiation up to 2×10^{13} *ions* cm^{-2}. A bright field electron micrograph shows that, after irradiation at 80 K at very high fluences, *anisotropic growth* occurs (figure 10(b)) [1–4], and induces important deformations which are visible near the central hole of the sample. No crystalline diffraction rings are visible on the electron diffraction pattern (figure 10(a)), whereas two rings, called hereafter $\mu 6$ and $\mu 7$ (figure 13) are visible on the microdiffraction pattern (figure 10(c)). Both of them correspond to radial distances located inside the diffuse rings A1 and A2, which explains why they are not visible in figure 10(a).

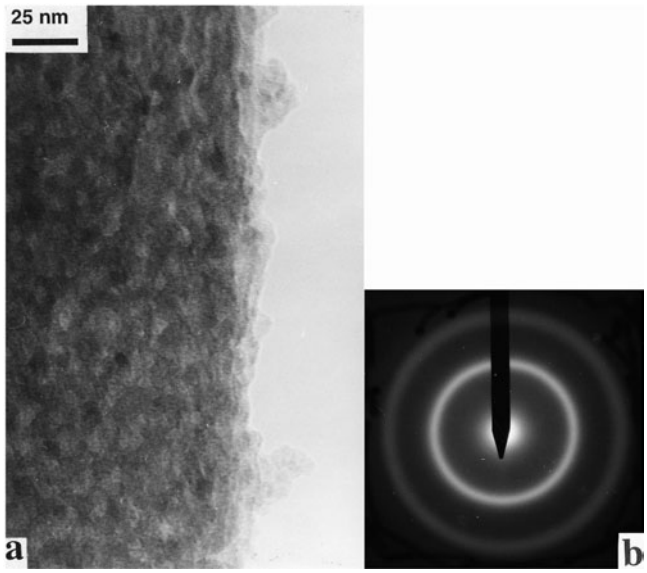

Figure 11. Bright field transmission electron micrograph (a) of a $Fe_{73.5}Cu_1Nb_3Si_{13.5}B_9$ amorphous sample irradiated at normal incidence at 300 K with 0.7 GeV Pb ions up to a fluence of 2×10^{12} ions cm^{-2}. No crystalline rings are visible on the corresponding electron diffraction pattern (b).

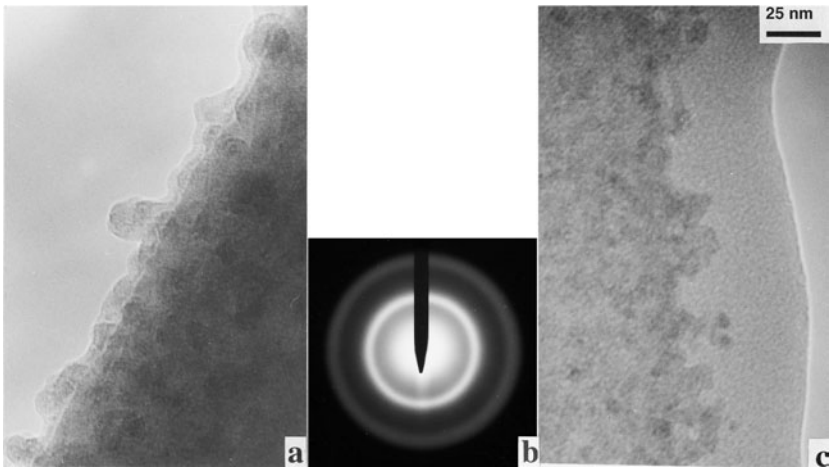

Figure 12. Bright field transmission electron micrographs (a) and (c) of an $Fe_{73.5}Cu_1Nb_3Si_{13.5}B_9$ amorphous sample irradiated at normal incidence at 300 K with 0.7 GeV Pb ions up to a fluence of 8×10^{12} ions cm^{-2}. No crystalline rings are visible on the corresponding electron diffraction pattern (b).

3.3.2. Irradiation at 300 K with 700 MeV lead ions. Figures 11(a) and 12(a) show that strong anisotropic growth is observed on the edges of samples irradiated at room temperature up to fluences of 2×10^{12} and 8×10^{12} ions cm^{-2} respectively. Figure 12(c) shows another frequently observed image of the outward flow of matter into the central hole of the sample: the edge of the sample has an amorphous structure, whereas in thicker sample regions the sample surface is covered with small crystallites. This result will be discussed below. On the corresponding

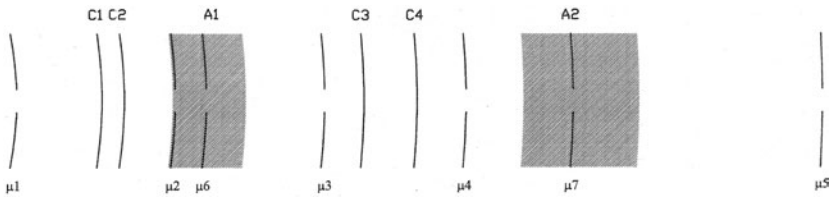

Figure 13. Schematic representation of the observed diffraction rings: A1 and A2 from the amorphous matrix (figure 1), C1–C4 from the crystalline matter formed during the irradiation (figures 2, 5, 7, 8, 13), $\mu 1$–$\mu 7$ from the crystalline material observed on microdiffraction patterns (figures 8, 12). Some of them ($\mu 2$, $\mu 6$ and $\mu 7$) are located inside the diffuse amorphous rings. The positions of all diffracted rings are drawn to scale, with respect to the measured radii on the various electron diffraction patterns.

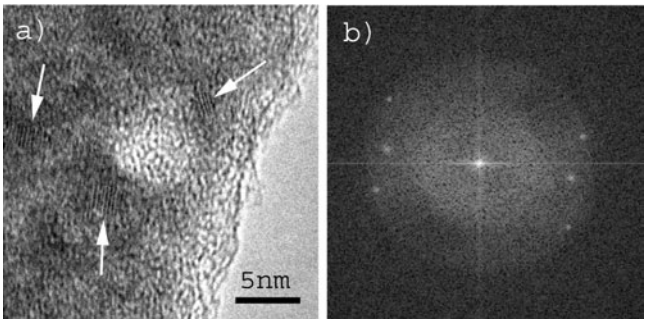

Figure 14. High-resolution transmission electron micrograph of an isolated damaged region in an $Fe_{73.5}Cu_1Nb_3Si_{13.5}B_9$ sample irradiated with 5 GeV Pb ions at 80 K up to a fluence of $\Phi = 1 \times 10^{11}$ cm^{-2} (a). The corresponding FT plot is shown in (b). Nanocrystallites are indicated by arrows.

electron diffraction patterns (figures 11(b) and 12(b)), once again, as in figure 10(a), no sign of crystallization can be detected.

3.4. High-resolution electron microscopy

Figure 14(a) presents an HRTEM micrograph of an isolated damaged region from a sample irradiated with 5 GeV Pb ion at 80 K. The experimental image was taken at the Scherzer defocus ($D_f = -90$ nm). We observe that the track diameter is 6–8 nm and that the track core is amorphous. Nanocrystallites, with a size ranging between 1 and 4 nm, are observed around the ion track. This result agrees with the conclusions deduced from the dark field image shown in figure 6(c). The micrograph also shows that nanocrystallites are formed even as far as 10 nm from the ion path. The corresponding Fourier transform (FT) plot shows the presence of diffraction spots characteristic of Fe_2B and $Fe_{23}B_6$ crystalline structures (figure 14(b)). These spots correspond respectively to the C1 and C2 crystalline rings in figure 13. The few diffraction spots observed in the FT plot (figure 14(b)) are due to the very local information obtained from FT analysis, where only a few crystallites contribute to the FT image.

4. Discussion

In order to understand the mechanism of irradiation-induced nanocrystallization, it is useful to review some aspects of the relaxation of the energy deposited into the target during the slowing

down of a swift heavy ion through matter. Interaction of high-energy heavy projectiles with matter strongly depends on the energy of the particle and on the properties of the target. Energy loss of swift heavy ions occurs through elastic collisions with target nuclei and through inelastic collisions with target electrons. The slowing down of ions due to elastic collisions with the nuclei dominates at low energy, e.g. at the end of the ion range. Inelastic processes, which lead to electronic excitation and ionization of the target atoms along the path of the projectiles, strongly prevail at very high energies. The resulting damage depends strongly on the target material and on the energy deposited along the ion path. As the ion–matter interaction in the electronic excitation regime is an ultrafast process, we deal with phenomena which are highly out of equilibrium. Two models are often used to account for experimental observations:

(i) The Coulomb explosion model mainly considers the ionization of the atoms located in the vicinity of the ion path [17–20]. The resulting electrostatic potential energy is converted into atomic kinetic energy without a significant increase of the local temperature.
(ii) Thermal spike models which deal with the conversion of the energy of the ejected δ-electrons into the atomic subsystem via electron–phonon or electron–atom interaction and lead to a local 'temperature' increase within 10^{-12} s [21–23].

This temperature increase is not easy to define or to evaluate quantitatively and leads to contradictory estimates in the literature [23–26]. It is followed by a rapid quenching (10^{12}–10^{14} K s^{-1}) within 10^{-9} s.

All the experimental results concerning the latent track diameter measured after monoatomic ion irradiation, are shown in figure 15 as a function of the linear rate of electronic energy deposition, S_e. Previous results demonstrated that there is not a simple relation between S_e and track formation. For a given projectile, the track diameter increases with ion velocity, reaches a maximum value, and then decreases again beyond the maximum stopping power, giving rise to a hook-like curve [27]. This effect is often called velocity effect [28], indicating that for the same S_e, slow projectiles induce larger diameter tracks than faster projectiles due to the differences in the density of energy deposited by low- and high-velocity ions. The higher the δ-electron velocity, the larger the range, and the lower the energy density deposited on the electronic system as the ion-damaged volume scales with the range of the δ-electrons. The velocities of 0.7 and 5 GeV of Pb ions are, respectively, on the low-velocity and on the high-velocity side of the stopping power curve. We observe that, for almost similar linear rates of energy deposition into electronic excitation (40–50 keV nm^{-1}), 0.7 GeV Pb ions will damage a much larger region than 5 GeV Pb ions. This result can be understood in the frame of the role of the velocity effect in the damage creation process.

Figure 15 also shows that the efficiency in damage creation is a function of the temperature. The measured diameters of latent tracks after irradiation with 5 GeV lead ions are about 7.2 nm for the irradiation at 80 K and 8.2 nm for the irradiation at 300 K, which corresponds to a change of about 14%. This indicates the importance of the atomic mobility in damage creation.

The averaged radii of the different rings measured on several diffraction patterns allow us to calculate the corresponding interplanar distances of the nanocrystallites. These distances are then compared with the corresponding interplanar distances of the main crystalline phases that appear during thermal annealing of $Fe_{73.5}Cu_1Nb_3Si_{13.5}B_9$ alloy. A schematic drawing of the relative positions of all diffraction rings is shown in figure 13. The two wide grey rings A1 and A2 represent the diffuse diffraction halos from the amorphous matrix. The four continuous lines, labelled C1–C4, give the relative positions of the thin circles characteristic of the crystalline matter that is formed during the irradiations (figures 2, 4, 5, 7, 8). The seven dashed lines, μ1–μ7, correspond to the diffraction lines originating from crystalline matter which are observed in microdiffraction diagrams (figures 8, 10). The most probable

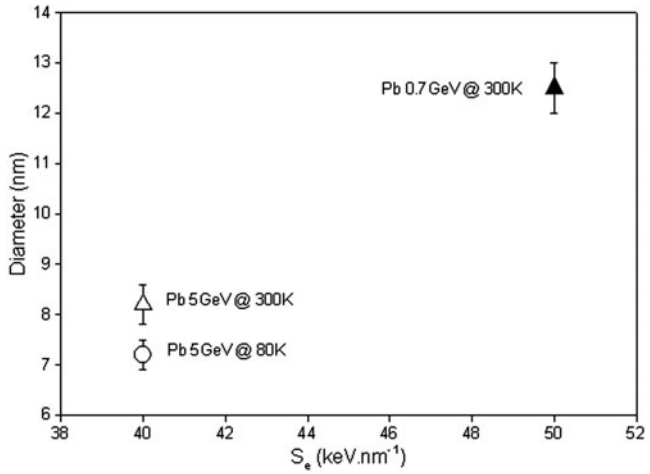

Figure 15. The plot shows the evolution of the inner track diameter as a function of the linear rate of energy deposited in electronic processes, S_e, and of the irradiation temperature.

crystalline phases from which the diffraction rings originate have been reported in table 2, when they could be unambiguously determined. This identification shows that the observed distances agree reasonably well with the interplanar distances of face centred cubic $Fe_{23}B_6$ (and for one line with those of tetragonal Fe_2B). However, since some strains could exist in the small boride grains, this could lead to significant deviations of the interplanar distances from the theoretical ones. It seems nevertheless that we *do not observe any evidence of the formation of Fe(Si) phase, and could mainly identify the formation of fcc* $Fe_{23}B_6$ *and to a smaller extent of tetragonal* Fe_2B.

An insight into irradiation-induced crystallization is obtained from HRTEM micrographs. Figure 14 shows that the nanocrystallization does not occur in the close vicinity of the ion path (track core), which remain amorphous, but mostly around the track core. HRTEM micrographs also shows that nanocrystallites are present at distances as large as 10 nm from the trajectory of the ion.

The fact that the track core remains amorphous can be interpreted as the consequence of the rapid cooling down (10^{12}–10^{14} K s^{-1}) of the track core region following the thermal excitation of the electrons close to the ion path. This very rapid quenching is several orders of magnitude larger than the normal quenching rate obtained with the melt-spun technique ($\sim 10^6$ K s^{-1}), and could prevent the formation of the crystalline phase. On the other hand, if the irradiation-induced crystallization was solely a thermally activated process we should find the same crystalline phases as observed during the thermal treatment. In particular, we would expect to observe the phase corresponding to the primary crystallization: specifically the Fe(Si) phase. Nevertheless, not only was no evidence found for the formation of the Fe(Si) phase, but we also mainly observed the precipitation of borate compounds, which are typical of the second crystallization step. Thus, we conclude that, if a thermal effect is active during the electronic relaxation, it cannot be the only process behind the origin of the observed nanocrystallization.

Finally, the experimental observation that at high irradiation fluences the crystalline rings in the electron diffraction patterns become weaker, may be understood either as (i) a sputtering of nanocrystallites formed on the sample surface or (ii) a re-amorphization of the pre-existing nanocrystallites under subsequent electronic energy deposition. During swift

heavy ion irradiation a fraction of the incident energy is transferred to the target atoms, resulting in the ejection of surface atoms into the vacuum. As the probability for an ion to pass close to an already formed latent track is proportional to the irradiation fluence, above a critical fluence the effect of formation of a new latent track will result in the sputtering of pre-existing nanocrystallites at the surface.

As nanocrystallites are in a metastable phase, we can suppose that a subsequent deposition of a high density of energy in electronic processes may induce the re-amorphization of the crystallites.

Both processes result in a weakening of the diffraction pattern signal when increasing the irradiation fluence.

5. Conclusion

The main results of irradiation with monoatomic heavy ions are reported in table 2 and can be summarized as follows:

(a) Surface deformations are always observed.
(b) The core of the *tracks* remains amorphous: the diameter depends on the irradiation conditions. For irradiation with lead ions, and for $S_e \sim 40$ keV nm^{-1}, this diameter increases from 7 to 8 nm when the irradiation temperature increases from 80 to 300 K. At the same irradiation temperature (300 K), it strongly increases from 8 to 12 nm when S_e changes from 40 to 50 keV nm^{-1}.
(c) Anisotropic growth is observed after irradiations at 80 and at 300 K. Because the headlands are heterogeneously distributed on the edge of the sample, we suppose that anisotropic growth does not take place as a uniform movement of matter, which moves toward the surface, but rather as a localized mass movement.
(d) After irradiation at high fluences the crystalline rings in the electron diffraction patterns become weaker or even disappear.
(e) High electronic excitation-induced crystallization cannot be a purely thermal process.

Acknowledgments

The authors would like to thank all the staff of the CIRIL laboratory and in particular J M Ramillon for his very efficient help.

References

[1] Klaumünzer S, Schumacher G, Rentzsch S, Vogl G, Soldner L and Bieger H 1982 *Acta Metall.* **30** 1493
[2] Audouard A, Balanzat E, Fuchs G, Jousset J C, Lesueur D and Thomé L 1987 *Europhys. Lett.* **3** 327
Audouard A, Balanzat E, Fuchs G, Jousset J C, Lesueur D and Thomé L 1989 *Nucl. Instrum. Methods* B **39** 18
[3] Klaumünzer S, Li C, Loffler S, Rammensee M, Schumacher G and Neitzert H Ch 1989 *Radiat. Eff. Defects Solids* **108** 131
[4] Audouard A, Toulemonde M, Szenes G and Thomé L 1998 *Nucl. Instrum. Methods* B **146** 233
[5] Hou M D, Klaumünzer S and Schumacher G 1990 *Phys. Rev.* B **41** 1144
[6] Audouard A, Balanzat E, Jousset J C, Lesueur D and Thomé L 1993 *J. Phys.: Condens. Matter* **5** 995
[7] Dunlop A, Jaskierowicz G, Rizza G and Kopcewicz M 2003 *Phys. Rev. Lett.* **90** 015503
[8] Yoshizawa Y, Oguma S and Yamauchi K 1988 *J. Appl. Phys.* **64** 6044
[9] Gorria P, Garitaonandia J S and Barandiaran J M 1996 *J. Phys.: Condens. Matter* **8** 5925
[10] Kataoka N, Inoue A, Masumoto T, Yoshizawa Y and Yamauchi K 1989 *Japan. J. Appl. Phys.* **28** 1820
[11] Kulik T and Hernando A 1995 *Mater. Sci. Forum* **179–181** 587
[12] Dunlop A, Jaskierowicz G and Della Negra S 1997 *C.R. Acad. Sci.* IIb **325** 397

[13] Dunlop A, Henry J and Jaskierowicz G 1998 *Nucl. Instrum. Methods* B **146** 222
[14] Guinier A 1964 *Théorie et Technique de la Radiocristallographie* (Paris: Dunod) p 452
[15] Hampel G, Pundt A and Hesse J 1992 *J. Phys.: Condens. Matter* **4** 3195
[16] Baudin K, Brunelle A, Chabot M, Della-Negra S, Depauw J, Gardès D, Hakansson P, Le Beyec Y, Billebaud A, Fallavier M, Remillieux J, Poizat J C and Thomas J P 1994 *Nucl. Instrum. Methods* B **94** 341
[17] Fleischer R L, Price P B and Walker R M 1965 *J. Appl. Phys.* **36** 3645
[18] Bitensky I S and Parilis E S 1987 *Nucl. Instrum. Methods* **21** 26
[19] Johnson R E, Sundqvist B U R, Hedin A and Fenyö D 1989 *Phys. Rev.* B **40** 49
[20] Lesueur D and Dunlop A 1993 *Radiat. Eff. Defects Solids* **126** 163
[21] Seitz F and Koehler J S 1956 *Solid State Phys.* **2** 305
[22] Chadderton L T and Montagu-Pollok H M 1969 *Proc. R. Soc.* A **274** 239
[23] Toulemonde M, Dufour C and Paumier E 1992 *Phys. Rev.* B **46** 14362
[24] Martynenko Yu V and Yavlinskii Yu N 1983 *Sov. Phys.—Dokl.* **28** 391
[25] Miotello A and Kelly R 1997 *Nucl. Instrum. Methods* B **122** 458
[26] Volkov A and Borodin V A 1998 *Nucl. Instrum. Methods* B **146** 137
[27] Jensen J, Dunlop A, Dalla-Negra S and Toulemonde M 1998 *Nucl. Instrum. Methods* B **146** 412
[28] Meftah A, Brisard F, Costantini J M, Hage-Ali M, Stoquert J P, Studer F and Toulemonde M 1993 *Phys. Rev.* B **48** 920